Additive Manufacturing 35 (2020) 101293

Contents lists available at ScienceDirect

Additive Manufacturing

journal homepage: www.elsevier.com/locate/addma

Research Paper

Morphological and microstructural investigation of the non-planar interface formed in solid-state metal additive manufacturing by additive friction stir deposition

Mackenzie E.J. Perry[a,b], R. Joey Griffiths[a], David Garcia[a], Jennifer M. Sietins[b], Yunhui Zhu[c], Hang Z. Yu[a,*]

[a] Department of Materials Science and Engineering, Virginia Tech, Blacksburg, VA 24061, USA
[b] CCDC Army Research Laboratory, Aberdeen Proving Ground, MD 21005, USA
[c] Department of Electrical and Computer Engineering, Virginia Tech, Blacksburg, VA 24061, USA

ARTICLE INFO

Keywords:
Additive friction stir deposition
X-ray computed tomography
Interface
Material flow
Dynamic recrystallization

ABSTRACT

Additive friction stir deposition (AFSD) is an emerging solid-state metal additive manufacturing technology renowned for strong interface adhesion and isotropic mechanical properties. This is postulated to result from the material flow phenomena near the interface, but experimental corroboration has remained absent. Here, we seek to understand the interface formed in AFSD via morphological and microstructural investigation, wherein the non-planar interfacial morphology is characterized on the *track-scale (centimeter scale)* using X-ray computed tomography and the material deformation history is explored by microstructure mapping at the interfacial regions. X-ray computed tomography reveals unique 3D features at the interface with significant macroscopic material mixing. In the out-of-plane direction, the deposited material inserts below the initial substrate surface in the *feed-rod zone,* while the substrate surface surges upwards in the *tool protrusion-affected zone*. Complex 3D structures like fins and serrations form on the advancing side, leading to structural interlocking; on the retreating side, the interface manifests as a smooth sloped surface. Microstructure mapping reveals a uniform thermo-mechanical history for the deposited material, which develops a homogeneous, almost fully recrystallized microstructure. The substrate surface develops partially recrystallized microstructures that are location-dependent; more intra-granular orientation gradients are found in the regions further away from the centerline of the deposition track. From these observations, we discuss the mechanisms for interfacial material flow and interface morphology formation during AFSD.

1. Introduction

Additive friction stir deposition (AFSD) is an emerging solid-state additive process with great promise for large-scale additive manufacturing, cladding, and repair of metals and composites [1,2]. It joins the friction stir principle with material feeding to facilitate site-specific, solid-state deposition [3–5]. During deposition, the feed material in the form of a solid feed-rod is delivered through a hollow tool head and rotates rapidly together with it; the dynamic contact at the feed-rod and substrate interface results in frictional heating. The softened feed material is then yielded by the compression from the feeding apparatus and expands below the tool head. The shear force from the bottom surface of the tool head further causes the expanded material to flow and spread between the tool head and substrate. During the deposition process, the material undergoes severe plastic deformation at high shear strain rates [6–9], which results in additional volumetric self-heating [2,10–12]. In-plane motion of the tool head leads to deposition of a continuous track of material onto the substrate, which can be built up layer-by-layer to form a 3D part.

Beam-based metal additive manufacturing technologies, such as powder bed fusion and directed energy deposition [13–18], typically lead to anisotropic mechanical behavior in the as-printed state due to weak interfacial bonding. For example, anisotropic tensile elongation properties have been observed in Ti-6Al-4 V parts fabricated using directed energy deposition [19]. The ductility and the fracture mechanisms in Ti-6Al-4 V parts printed by selective laser melting have been found to be dependent on the build direction [20]. In contrast, AFSD can form high-quality interfaces with excellent out-of-plane mechanical

* Corresponding author.
E-mail address: hangyu@vt.edu (H.Z. Yu).

https://doi.org/10.1016/j.addma.2020.101293
Received 22 December 2019; Received in revised form 9 April 2020; Accepted 26 April 2020
Available online 11 May 2020

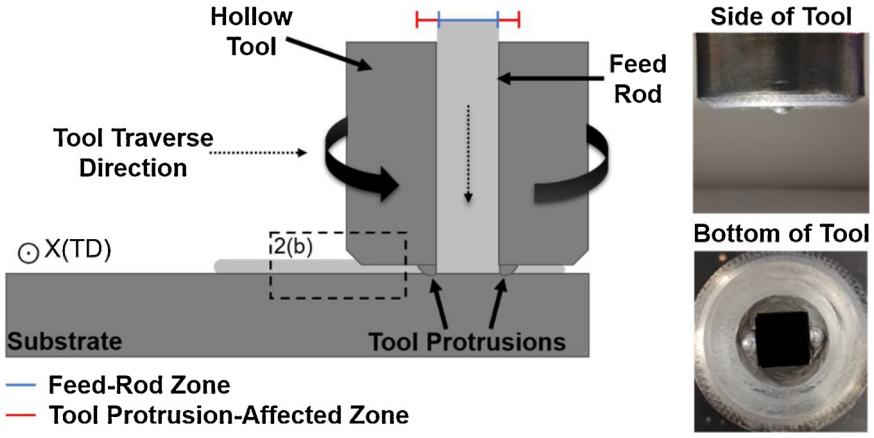

Fig. 1. A schematic of the additive friction stir deposition (AFSD) process. TD = transverse direction. Pictures of the side view and bottom view of the tool are also included.

properties in the as-printed state, as seen in recent AFSD studies on WE43 [21], AA 2219 [9], and IN625 [12,22] alloys. As a result, the tensile or compressive strength measured along the out-of-plane direction can be comparable to that measured along in-plane directions. The good interface properties in AFSD are also confirmed through bending tests and basic inspection. For instance, no delamination occurs at the interface in Cu-Nb and Cu-Ta bilayer structures even after significant bending [1]. After the repair of high strength Al alloys using AFSD, optical microscopy reveals no voids or kissing bonds between the deposited material and base structures [23].

The good interface quality from AFSD is postulated to originate from the interaction between the deposited material and the substrate (or between neighboring layers) [1], which is associated with the material flow and deformation phenomena. Material flow in friction stir welding (FSW) has been extensively investigated in literature [6,8,24–41], wherein the material mixing and weld microstructure are linked to the processing parameters and tool profiles. Compared to FSW, AFSD has a different geometric configuration without penetrating pins; instead, new material is continually fed into the deposition zone and interacts with the substrate, creating a fundamentally different system to investigate. In addition, the deposited material lies on top of the substrate without mechanical constraint in the lateral direction, as opposed to the strong lateral constraint imposed by the workpieces onto the stir zone material in FSW. Moreover, the joining in FSW mainly relies on the material flow around the pin, but in AFSD the interface quality is more determined by the material flow along the vertical direction. Although AFSD follows the same friction stir principle as FSW, the salient differences above necessitate a systematic investigation into the interfacial material flow and the consequential interface morphology in AFSD—not only to reveal the fundamentals of material flow in this new configuration but also to understand the origins of good interface quality.

Here, we present the first comprehensive experimental study on the interface formed in AFSD, with the aim to understand its 3D morphology, its formation process, and the associated dynamic microstructure evolution in the interfacial regions. Given the complex morphological features of the interface in AFSD, 2D characterization of the cross-section, e.g., using optical or electron microscopy, is insufficient. Instead, 3D characterization techniques employing penetrating beams like neutrons or X-rays are essential. With a good balance of spatial resolution and field of view, X-ray computed tomography has been employed for 3D morphological characterization in this work. Given that AFSD can be viewed as a hot working process with the resultant microstructure governed by the material deformation and thermal history, mapping the microstructural features in the interfacial regions—such as grain size, texture, and grain boundary misorientation—can shed additional light on interfacial material deformation and flow.

The morphological and microstructural investigation in this work focuses on the interface formed in a dissimilar Al alloy system, involving an Al-Cu alloy (AA 2024) deposited onto an Al-Mg-Si alloy (AA 6061). This material system is chosen because AA 2024 and AA 6061 have sufficient X-ray absorption contrast to be distinguished from each other. In addition, the two alloys have comparable mechanical properties [42,43] to ensure a high-quality deposition and to effectively reveal the interfacial material flow characteristics of *homogeneous* material deposition.

2. Experimental procedures

AFSD of a single layer of AA 2024 was carried out using a MELD R2 machine [44]. The average single-layer deposition thickness of AA 2024 was 1.65 mm and the AA 6061 substrate thickness was 6.35 mm. For AFSD, there have been a few tool designs, including tools that are completely flat on the bottom and tools with small protrusions. Flat tools allow for deposition of thinner layers, while tools with protrusions can promote deep material mixing. For this study, the bottom surface of the tool head was flat except for two small protrusions (height ~ 1.5 mm) near the edge of the opening for feed material. During deposition, the protrusions were partially (~ 0.5 mm deep) inserted into the substrate, in order to promote vertical mixing between the deposited material and the substrate. It should be noted that the spacing between the tool head and substrate was set to be ~ 1 mm, which was less than the final deposition thickness of 1.65 mm. This was caused by the unconstrained upward flow when the material exits the deposition zone on the trailing side, as elaborated in Section 3.1. A schematic of the tool head and feed-rod geometry is shown in Fig. 1, wherein the area covered by the feed-rod during deposition is defined as the 'feed-rod zone' and the area covered by tool protrusions is defined as the 'tool protrusion-affected zone'. Also shown in Fig. 1 are the side view and bottom view of the tool. The deposition was carried out at a tool head rotation rate of Ω = 300 RPM and an in-plane velocity of V = 2.00 mm/s. The material feed rate is R = 0.85 mm/s. The ratio of feed rate to in-plane velocity is an important value for obtaining good print quality. Layer thickness and track width depend on this ratio in addition to the material system and tool rotation rate. A laser confocal microscope (Olympus LEXT MM6-ASPS) was used to visualize the macrostructure of the deposit.

The 3D interfacial morphology was characterized using X-ray computed tomography. For X-ray scanning of the entire deposition track (i.e., track-scale), the specimen was scanned using a North Star X5000 CT with a voxel size of 33.1 μm and a voltage of 120 kV. For X-

ray scanning of a smaller volume with a higher resolution, the scans were conducted using a Zeiss Xradia 520 Versa MicroCT with a voxel size of 9.85 μm and a voltage of 60 kV. The 3D volumes were reconstructed using the X-ray projection images and then visualized using CTVox and VGStudio MAX software.

For microstructure characterization, the samples were cut perpendicular to the longitudinal direction so that the transverse cross-section could be examined. The samples were ground using silicon carbide papers (400, 600, and 1200 grit), polished using polycrystalline diamond suspensions, and finished with 0.02 μm colloidal silica suspension. Energy dispersive spectroscopy (EDS) and electron backscatter diffraction (EBSD) measurements were conducted using a FEI NOVA NanoSEM 600 field emission scanning electron microscope. The chemical composition was analyzed with the attached Octane Elite EDS detector, and EBSD mapping was conducted at a step size of 0.5 – 0.9 μm. To avoid artificial boundaries from orientation noise, a minimum of 2 degrees was set for boundary misorientation. The boundaries between 2–15 degrees were defined as low angle boundaries (LABs) and the boundaries above 15 degrees were defined as high angle boundaries (HABs). The area of each individual grain was measured with the OIM software; the reported diameter was calculated as if that area formed a perfect circle.

3. Morphological investigation using X-ray computed tomography

3.1. General appearance and surface features

The general appearance of the AA 2024 deposit is shown in Fig. 2(a) from the top view, i.e., the X–Y plane projection (see the figure for definitions of X-, Y-, Z- directions). The surface of the deposit shows a typical “onion skin” feature, which has also been observed in FSW [45–48]. For AFSD with different sets of in-plane velocity V and tool rotation rate Ω, we find that the measured onion skin spacing always matches well with the calculated advance per revolution (APR). This consistency suggests that the onion skin is caused by the interaction between the tool edge and the top surface of the deposited material during each revolution of the tool. As the tool head moves forward, the top surface of the deposited material flows out of the deposition zone (i.e., the volume beneath the tool) from the trailing side, and the trailing edge of the tool head effectively mills an imprint into the deposited material. This effect is illustrated in Fig. 2(b). The coupling of tool head motion and the imprint effect results in an onion skin pattern on the top surface of the deposit. The unconstrained upward flow labeled in Fig. 2(b) also explains the discrepancy between the final deposition height (1.65 mm) and the spacing between the tool head and substrate (~1 mm). At the end of AFSD, the rotating tool is raised, and the feed-rod breaks off from the deposit, resulting in a rough circular area, as seen in Fig. 2(a). To compare, in FSW the end of welding leads to a large exit keyhole due to the removal of a non-consumable pin.

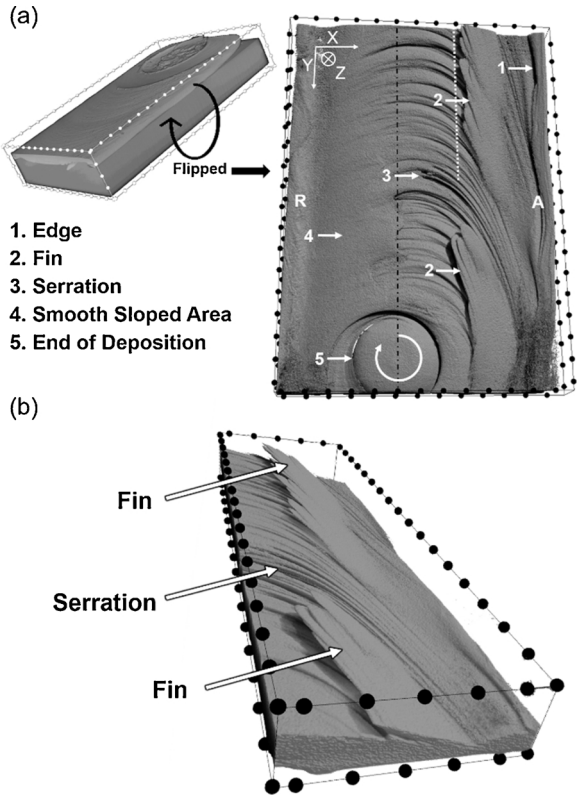

Fig. 3. X-ray computed tomography results for AA 2024 deposited onto AA 6061 via AFSD. (a) Underside of the deposited AA 2024 material with the substrate material removed and a few salient features highlighted. This is a flipped image so that the material flow is clockwise instead of counter-clockwise. A = advancing, R = retreating. The distance between each pair of dots is 2.5 mm. (b) An angled view of the deposited material on the advancing side to emphasize the fin structures.

3.2. Features of the 3D interfacial morphology

To unveil the 3D interfacial morphology, the substrate material is set to be transparent in the reconstruction volumes. This enables investigation of the underside of the deposited material (Fig. 3(a)), which is essentially a flipped image of the bottom surface of the deposit. The interface is noticeably not flat but exhibits a slope from the centerline to the two edges. On the advancing side, there are several unique 3D features. Near the advancing edge, there are thin, flat strips of the

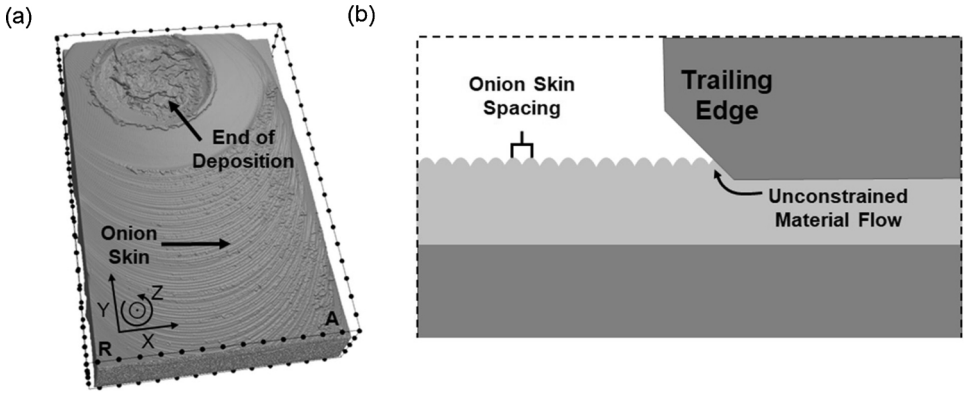

Fig. 2. (a) A top-down view of the deposited AA 2024 onto AA 6061 substrate based on X-ray computed tomography. A = advancing, R = retreating, X = transverse direction, Y = longitudinal direction, Z = build direction. The distance between each pair of dots is 2.5 mm. (b) Illustration of the ‘onion skin’ formation.

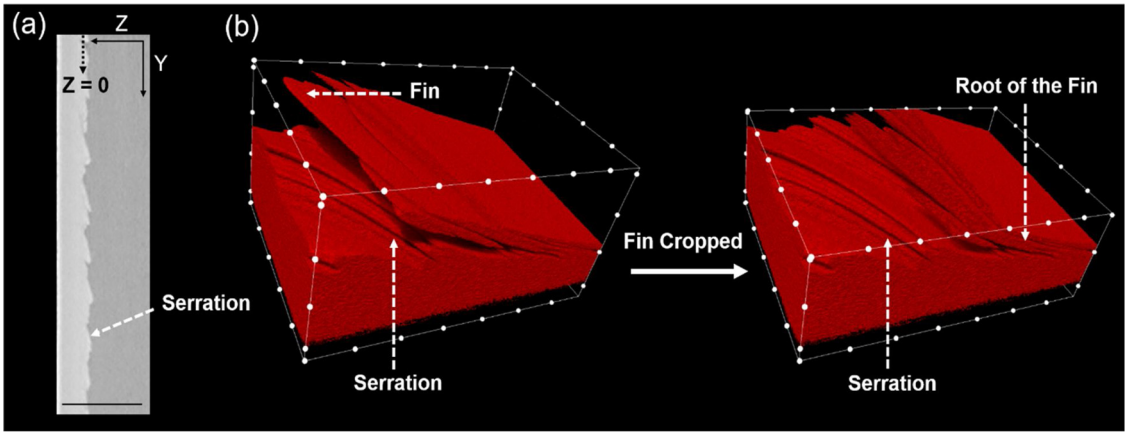

Fig. 4. High resolution X-ray computed tomography results for AA 2024 deposited onto AA 6061 via AFSD. (a) Serrations shown in a longitudinal cross-section (Y–Z plane) image. Light gray = AA 2024, Dark gray = AA 6061. The scale bar is 5 mm. (b) A full volume view of fins and serrations at a higher resolution and a cropped volume with the fins cropped. This shows the continuity of serrations throughout the fin-dominated area. The distance between each pair of dots is 1 mm.

deposited material accumulating right outside the tool protrusion-affected zone. A 3D view of these strips is shown in Fig. 3(b), revealing that they are not in parallel with the X–Y plane but rather are inclined away from the remaining deposited material. Given their shape shown in Fig. 3(b), we refer to these strips as 'fin' structures throughout this manuscript.

A series of periodic curves that start from the centerline and continue toward the advancing edge can also be seen in Fig. 3. In the longitudinal cross-section (Y–Z plane) shown in Fig. 4(a), such structures manifest as a series of jagged edges along the deposition track. They are thus referred to as 'serrations' in this manuscript. Near the advancing edge, the serrations are shadowed by the fin structure (see Fig. 3); however, the high-resolution X-ray tomography in Fig. 4(b) shows that the serrations extend all the way beyond the tool protrusion-affected zone, where they connect with the roots of the fins. Different from the advancing side, the retreating side of the interface lacks significant topological features, manifesting as a smooth sloped surface. A slice-and-view video showing the 3D view of the interface based on X-ray computed tomography can be found in Appendix A.

Fig. 5 shows a representative transverse cross-section (X–Z plane) of the interface. The Z-position of the initial flat substrate surface is set as Z = 0 mm. From this image, the deposited AA 2024 (light gray) plunges into the AA 6061 substrate (dark gray) and reaches Z = − 0.5 mm at the centerline, where the feed-rod is actively forced into the substrate by the feeding apparatus. This depth is very close to that reached by the tool protrusions during AFSD. Moving towards the edges of the feed-rod zone, the deposited material does not penetrate as deep beneath the substrate, whereas the substrate is forced above the initial substrate surface level. Between the tool protrusion-affected zone and the edges, the bottom of the deposited AA 2024 is seen to be well above the initial

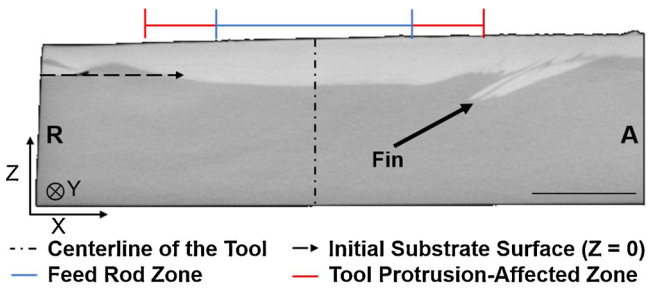

Fig. 5. A representative transverse cross-section (X–Z plane) of the deposit and substrate highlighting the bowl-shaped interface and macroscopic mixing. A = advancing, R = retreating, Light gray = AA 2024, Dark gray = AA 6061. The scale bar is 5 mm.

substrate surface. This gradual slope of the deposited material from the centerline gives rise to a "bowl-like" appearance of the interface. On the advancing side, between the tool protrusion-affected zone and the edge, the interface of the deposit develops a tilted shelf structure deeply penetrating the substrate, with a depth of Z_{FIN} = − 1.5 mm and a tilt angle of ~ 20° from the horizontal. This tilted shelf structure is the X–Z plane projection of the fin structure seen in Fig. 3. Remarkably, it is the fin structure, rather than the centerline of the feed-rod, that penetrates the deepest into the substrate (Z_{FIN} = −1.5 mm vs. $Z_{CENTERLINE}$ = − 0.5 mm).

3.3. Quantification of macroscopic material mixing

Based on more than 1000 collected X-ray cross-sectional images, we quantify the material distribution along the transverse direction (Fig. 6) and along the build direction (Fig. 7) using a self-developed MATLAB code. Fig. 6(a) shows a few representative longitudinal cross-section slices with different X coordinates. Fig. 6(b) plots the AA 2024 area percent along the X-direction, where each data point corresponds to the ratio of the measured area of AA 2024 to the combined area of AA 2024 and AA 6061 in a given slice. The shape of the plot agrees well with the features seen across the transverse cross-section in Fig. 5. At the retreating edge (X = 3 mm), the AA 2024 accounts for about 16 % of the total material. At X = 5 mm, the AA 2024 fraction drops to about 12 % because the substrate material rises above Z = 0 in this area. Further towards the advancing side (X > 5 mm), the AA 2024 fraction increases with the presence of serrations and fins, with a maximum fraction of 27.5 % reached at X = 22 mm. After that (X > 22 mm), there is a steep decline of the AA 2024 fraction towards the advancing edge. With the AA 2024 thickness of 1.65 mm and the AA 6061 thickness of 6.35 mm, the average fraction of AA 2024 should be 20.6 %, which matches the plotted results in Fig. 6(b). The non-flat interface and the observed 3D structures on the advancing side confirm that the substrate and deposited material are macroscopically mixed across the initial substrate surface level.

We next quantify the macroscopic mixing as a function of depth by comparing the horizontal cross-section (X–Y plane) images along the build direction. Fig. 7(a)–(f) show the horizontal cross-section images *above, at,* and *below* the initial substrate surface level. At Z > 0.75 mm, the deposit is a pure coating of AA 2024. Below that (e.g., Fig. 7(a) and (b)), the majority is still AA 2024, while the substrate AA 6061 starts to be observed close to the edges. At the initial substrate surface level, Z = 0 mm, there is about 60 % AA 2024, which lies within a central band enclosed by the tool protrusion-affected zone (see Fig. 7(c)). The serrations manifest as alternating curves of AA 6061/AA 2024 from the centerline to the advancing side. Below the initial substrate surface

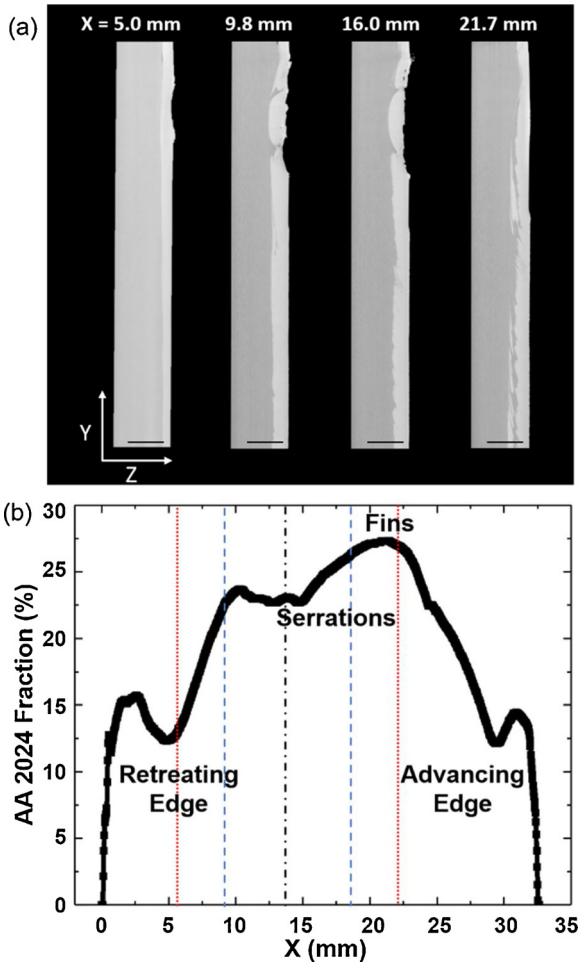

Fig. 6. (a) Longitudinal cross-section (Y–Z plane) images at chosen values in the X-direction. Light gray = AA 2024, Dark gray = AA 6061. The scale bar is 5 mm (b) Plot of the fraction of the deposited AA 2024 along the X-direction.

level (e.g., the case in Fig. 7(d)), the AA 2024 fraction continues to decline and only the serrations and fins exist. Close to Z = $Z_{CENTERLINE}$ = − 0.5 mm (see Fig. 7(e)), the deposited AA 2024 is mostly found within the feed-rod zone. Below that (e.g., the case in Fig. 7(f)), AA 2024 is only visible as the end tip of fins, which is along the edge of the tool protrusion-affected zone (on the advancing side). Fig. 7(g) quantifies the area percent of AA 2024 in the X–Y plane along the Z-direction, in which each data point corresponds to the AA 2024 area percent in an X–Y plane slice. The red shaded area represents the amount of substrate AA 6061 above Z = 0 mm and the green shaded area represents the amount of the deposited AA 2024 below Z = 0 mm. These shaded areas are a result of macroscopic material mixing in the vertical direction. Here, the latter is larger than the former because the tool protrusions insert into the substrate during deposition.

4. Microstructure mapping in the interfacial regions

4.1. General microstructural changes in the AA 2024 deposit and AA 6061 substrate after AFSD

Fig. 8 compares the microstructure of AA 2024 before and after AFSD. The IPF (inverse pole figure) coloring scheme and the reference directions are the same for each of the EBSD maps in this study. The microstructure of the as-received AA 2024 feed-rod is shown in Fig. 8(a), which is taken at the center of the feed-rod. A representative area in the transverse cross-section of AA 2024 after AFSD is shown in Fig. 8(b), which is taken within the feed-rod zone near the interface. It

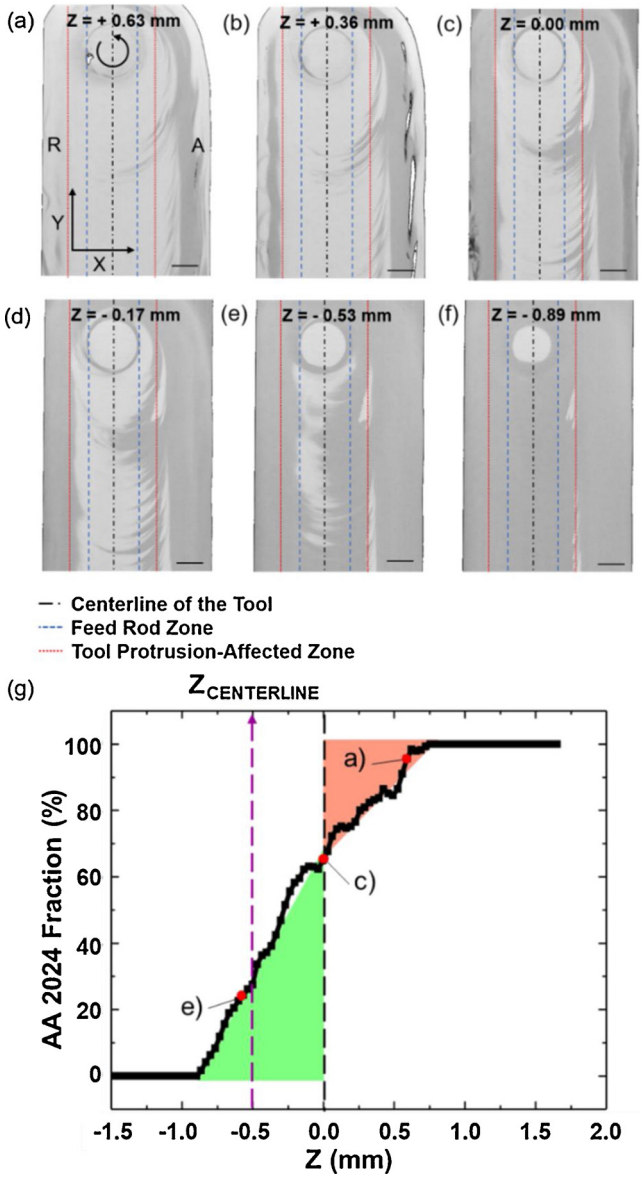

Fig. 7. Horizontal cross-section (X-Y plane) images at (a) Z = 0.63 mm, (b) Z = 0.36 mm, (c) Z = 0 mm, (d) Z = −0.17 mm, (e) Z = −0.53 mm, and (f) Z = −0.89 mm with the scale bar being 5 mm. A = advancing, R = retreating, Light gray = AA 2024, Dark gray = AA 6061. (g) Plot of the fraction of the deposited AA 2024 along the Z-direction.

is evident that the grain size after AFSD is considerably smaller than the original feed-rod, with the average grain size reduced from 57.2 μm to 4.9 μm. In addition, the grain structure in the as-received feed-rod consists of high aspect-ratio grains elongated along the drawing direction, whereas the deposited AA 2024 has mostly equiaxed grains. From the (100) and (111) pole figures, the feed material and the deposited AA 2024 are concluded to be weakly textured. Both *before and after* AFSD, the AA 2024 exhibits a misorientation distribution close to a Mackenzie distribution that would be observed in a randomly textured polycrystal [49].

Fig. 9(a) shows the microstructure of the as-received AA 6061 substrate; after AFSD, the microstructure of a representative portion of the deformed substrate close to the interface is shown in Fig. 9(b). Similarly, microstructure refinement is observed after AFSD with the average grain size reduced from 59.4 μm to 9.9 μm. Compared to the deposited AA 2024, the AA 6061 in the interfacial regions has a larger average grain size and displays varying degrees of color gradient in

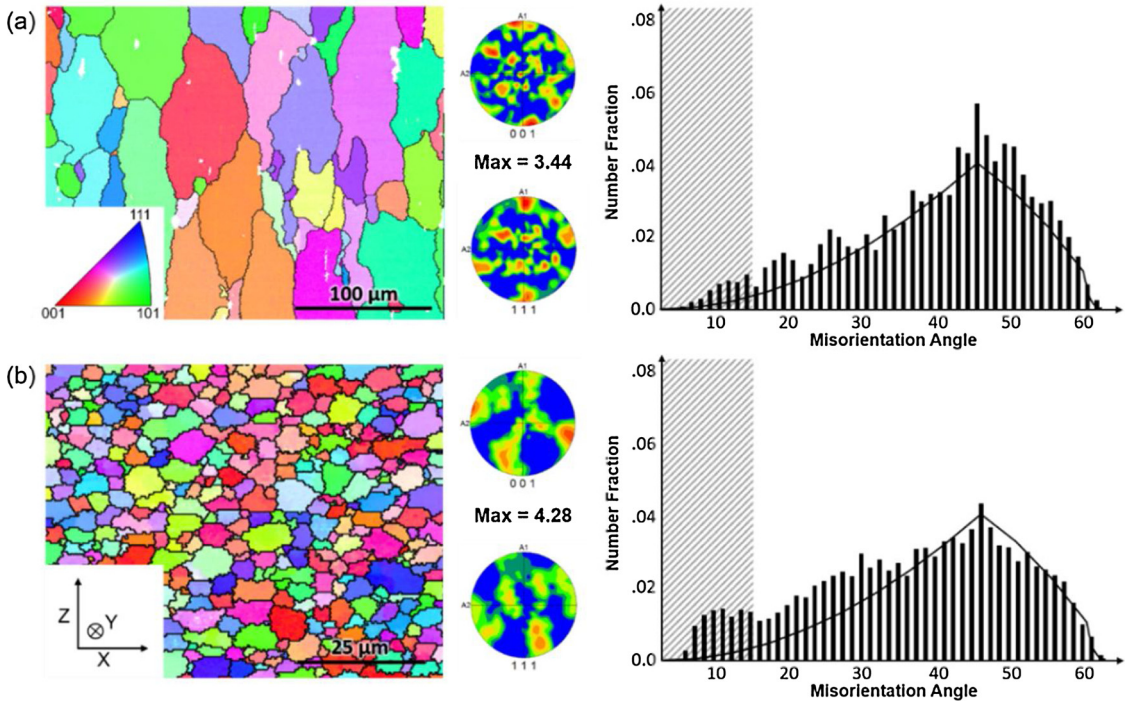

Fig. 8. Inverse pole figure (IPF) maps, pole figures, and misorientation angle distributions for (a) as-received AA 2024 feed material and (b) as-deposited AA 2024 near the interface. The IPF coloring scheme and the reference directions shown here are the same for each of the EBSD maps in this study.

individual grains. This suggests the presence of orientation gradients and geometrically necessary dislocations within the grains. The grain orientation in the AA 6061 substrate before AFSD is strongly textured with the (001) direction along the Y-direction as shown in Fig. 9(a). After AFSD, the rolling texture is no longer observed in the AA 6061 close to the interface, which exhibits a more random grain orientation distribution. Through AFSD, the maximum relative intensities in the pole figures of AA 6061 decrease from 34.67 to 7.44. In the as-received AA 6061 substrate, the misorientation distribution is skewed to the low angle grain boundary side, but a higher fraction of HABs is observed after AFSD.

4.2. Microstructure mapping

Fig. 10 is a composite of stitched images from confocal microscopy showing the transverse cross-section used for microstructure study.

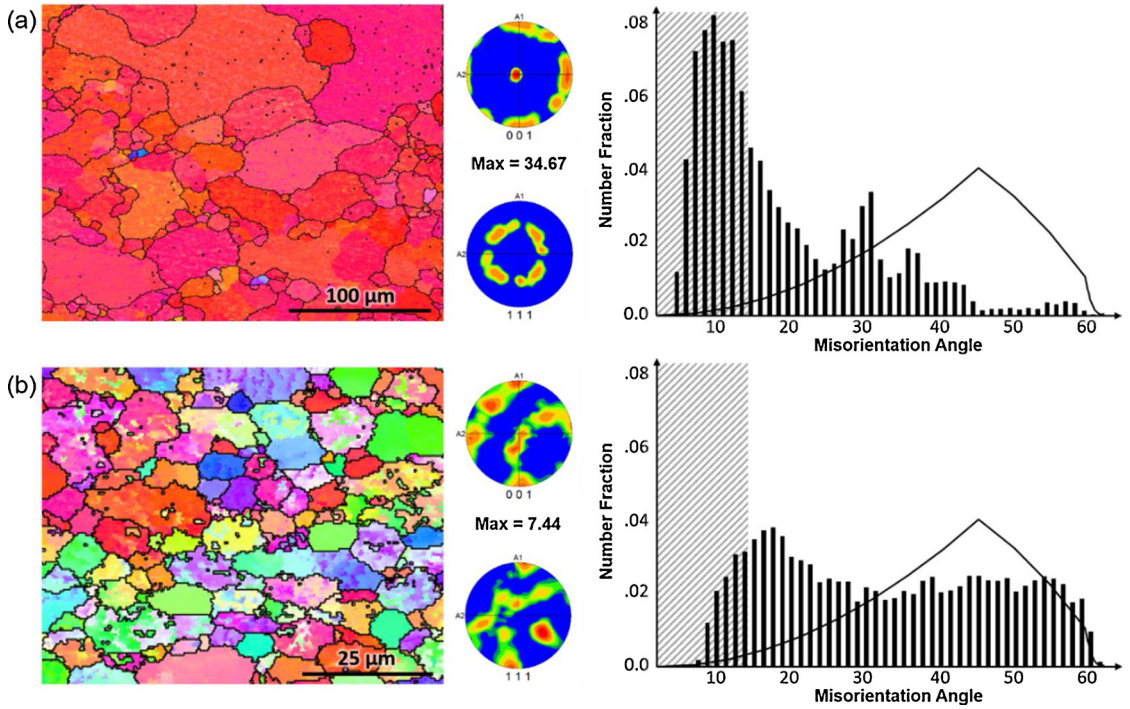

Fig. 9. Inverse pole figure maps, pole figures, and misorientation angle distributions for (a) as-received AA 6061 substrate material and (b) AA 6061 substrate near the interface after deposition. See Fig. 8 for IPF coloring scheme and reference directions.

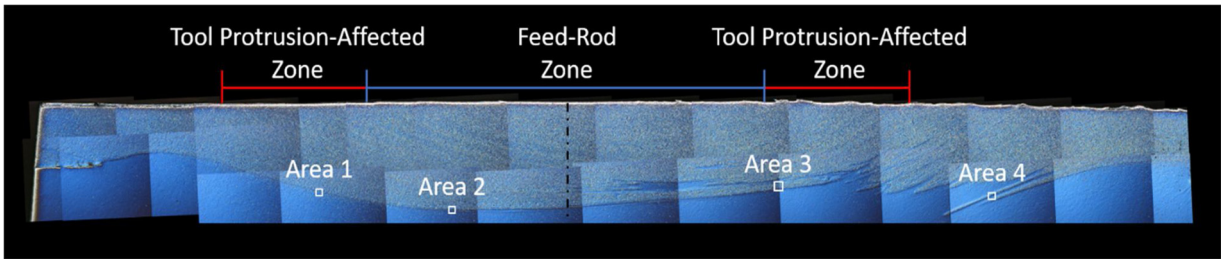

Fig. 10. Confocal microscopy results for AA 2024 (light blue) deposited onto AA 6061 (dark blue) via AFSD. A stitched image showing the transverse cross-section similar to that in Fig. 5. Four small areas (dimensions of hundreds of microns) with detailed microstructure characterization are labeled as 1, 2, 3, and 4.

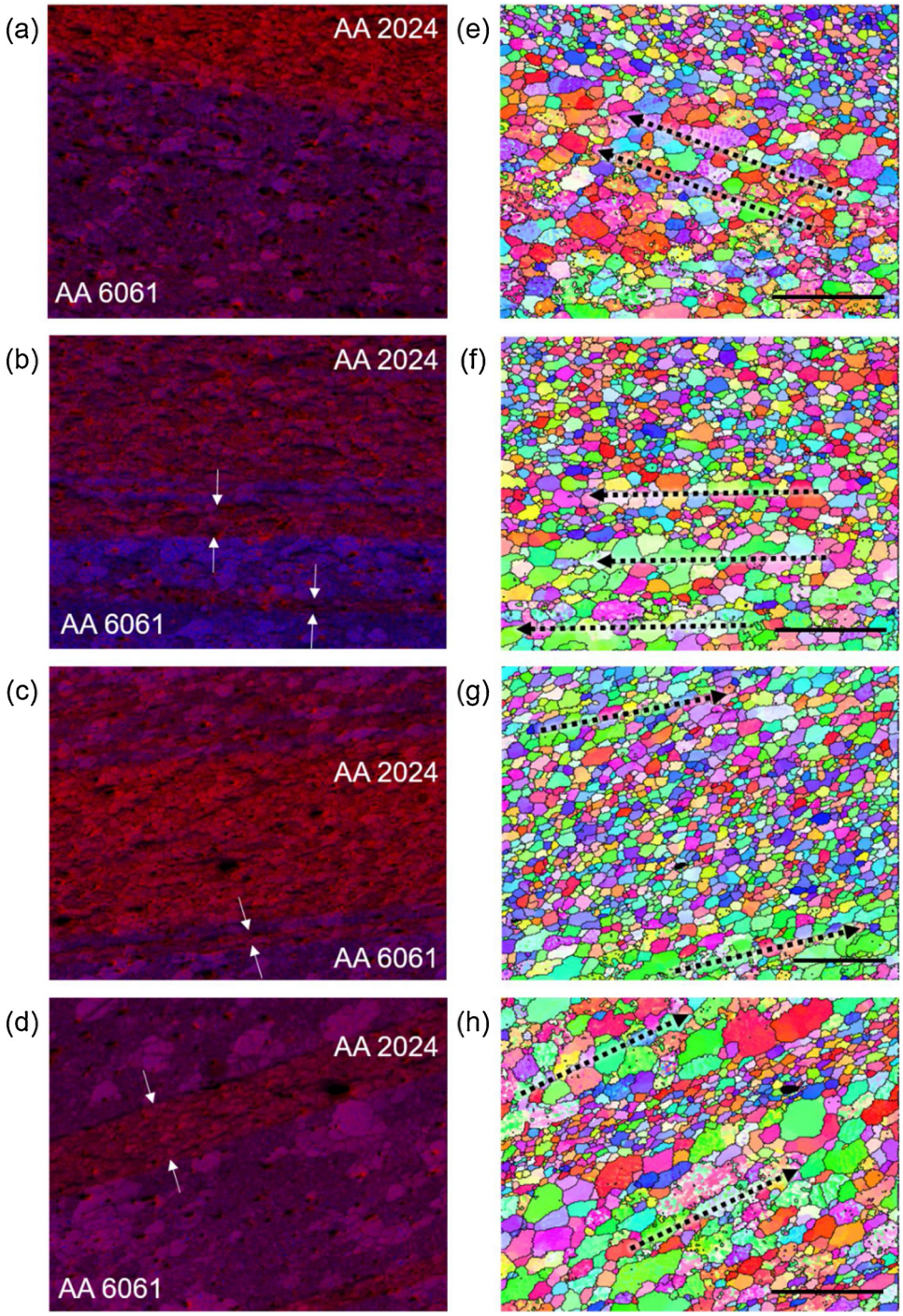

Fig. 11. (a)–(d) Energy dispersive spectroscopy (EDS) maps for Areas 1-4 where red areas represent AA 2024 and purple areas represent AA 6061. (e)–(h) Inverse pole figure (IPF) maps for Areas 1–4. Scale bars in subfigures are 50 μm.

Here, the lighter material is AA 2024 and the darker material is AA 6061. The regions below the blue and red lines represent the feed-rod zone and tool protrusion-affected zone, respectively. To compare the resultant microstructure at different locations in the transverse cross-section, four small interfacial regions with dimensions ~ hundreds of microns are subjected to detailed microstructure characterization. These areas are labeled as 1, 2, 3, and 4 in Fig. 10.

Fig. 11 shows the EDS ((a)–(d)) and IPF ((e)–(h)) mapping results of Areas 1–4. Each pixel in the EDS map represents aluminum counts, where the color scale varies from red to blue at the lowest and highest ranges, respectively. AA 2024 has a higher percentage of alloying elements, specifically 3.8–4.9 % copper, and therefore receives fewer aluminum counts than the AA 6061 substrates. For the EDS maps collected in this work, AA 2024 and AA 6061 are characterized by the red and purple regions respectively, as seen in Fig. 11. Complementary to the macroscopic mixing revealed by X-ray tomography, the EDS maps in Areas 2, 3, and 4 demonstrate intense material mixing at the mesoscopic level, showing lamellar banding between AA 2024 and AA 6061. This is highlighted by the white arrows shown in Fig. 11(b)–(d). From the corresponding IPF maps, the deposited AA 2024 in all areas develops fine, equiaxed microstructures and shows little color variation within individual grains. The uniformity of the microstructure suggests that all the deposited material has a similar thermomechanical history, which has led to the observed recrystallized microstructure. The grain size of the substrate AA 6061 is substantially larger than AA 2024 (9.9 vs. 4.9 μm), and the shape of the grain is generally more elongated. Interestingly, the long axis of these grains often aligns with the local interface, as highlighted by the black dashed arrows. For example, close to the center of the deposition, such as in Area 2 (Fig. 11(f)), the AA 6061 grains are elongated in the transverse direction. Closer to the edges of the deposition, such as in Area 1 and Area 4 (Fig. 11(e) and (h)), the AA 6061 grains are elongated at the same angle with the local interface seen in Fig. 10. This suggests that the dynamic microstructure evolution in AA 6061 is dictated by the shear deformation associated with the material flow at the interface.

Fig. 12(a)–(d) show the misorientation maps for Areas 1–4, in which LABs (misorientations between 2 and 15 degrees) are represented by red lines and HABs (misorientations larger than 15 degrees) are represented by black lines. In AA 2024, the fine equiaxed grains are separated by HABs with LABs occasionally observed in the grain interior. In AA 6061, LABs are prevalently observed inside individual grains that are more elongated. A closer examination of the LAB geometry is shown in Fig. 12(e), revealing several scenarios. In the first scenario (red circle), LABs appear as segments that completely cut across an elongated grain along the short-axis direction. In the second scenario (blue circle), a LAB manifests as a curved line that cuts out a small piece of a larger grain surrounded by HABs. In these two scenarios, further deformation would increase the misorientations between the subgrains via strain-induced HAB formation [50,51]. An interesting third scenario is highlighted by the black circles, in which a boundary is partially red and partially black. This transition from LAB to HAB in a single line suggests that the misorientation between subgrains increases gradually and continually, which is facilitated by dislocation accumulation and rearrangement in the presence of large deformation and dynamic recovery [52].

The above observations indicate that *continuous dynamic recrystallization*, which is characterized by dynamic recovery, subgrain formation, and strain-induced HAB formation, has occurred extensively in these two materials during AFSD. The difference lies in that the recrystallization is nearly complete in AA 2024; however, in AA 6061 the deformation is only sufficient to change a portion of LABs to HABs resulting in partial recrystallization. Grain refinement by continuous dynamic recrystallization is expected for high stacking fault energy materials like AA 2024 and AA 6061 with large deformation at elevated temperatures, which is consistent with the processing condition in AFSD [40,41,53,54].

Fig. 13(a)-(d) show the kernel average misorientation (KAM) distribution in Areas 1–4. Compared to the EDS maps in Fig. 11, the AA 2024 in all areas shows significantly lower KAM values than the AA 6061. This indicates that the orientation gradients and the geometrically necessary dislocations are effectively reduced as a result of recrystallization in the former. To better reflect the orientation gradients within individual grains, Fig. 13(e)-(h) and (i)-(l) show the maps of grain average misorientation (GAM) and grain orientation spread (GOS). GAM averages the local misorientation between neighboring pixels over each grain; GOS gives the grain-scale average value of the difference between the orientation of each pixel and the average orientation for that grain. Higher GAM and GOS values are observed in AA 6061 than AA 2024. More importantly, the GAM/GOS distribution in AA 2024 seems similar among Areas 1–4. However, there is an obvious correlation between the GAM/GOS values and locations in AA 6061; higher GAM/GOS values are found mostly in AA 6061 further from the center of the deposition in Areas 1 and 4. Since the intragranular orientation gradients result from incomplete recrystallization, we conclude that the AA 6061 in Area 2 and Area 3 have a higher degree of recrystallization than Area 1 and Area 4 [52].

5. Discussion

5.1. Mechanisms of the non-planar interface formation in AFSD

The interface in AFSD generally has a bowl shape with the center of the deposition showing significant interfacial mixing, which can be explained by analyzing the material flow at the interfacial regions (see Fig. 14(a)). First, with the compression from the feeding apparatus, the feed-rod inserts below the initial substrate surface, resulting in the presence of AA 2024 at $Z < 0$ mm within the feed-rod zone. Second, owing to the dynamic friction at the interface, the temperature rises and softens the surface of the substrate; however, the bulk of the substrate is still stiff and gives rise to a strong mechanical constraint. In reaction to the compression from the feed-rod, the softened substrate surface must bulge and surge above the interface (i.e., via outward and upward motion). Given the constraint from the tool protrusions, this motion mostly occurs outside the tool protrusion-affected zone, where AA 6061 is seen at $Z > 0$ mm. Essentially, a synergistic effect of the downward motion of the AA 2024 feed-rod in the feed-rod zone and the upward motion of the AA 6061 substrate outside the tool protrusion-affected zone leads to the intensive material mixing seen from X-ray computed tomography and confocal microscopy.

Another interesting feature of the interface is the asymmetry seen in the transverse cross- section. Figs. 2–7 show that the 3D interfacial structures only develop on the advancing side and the deposit is wider on the advancing side than the retreating side. This asymmetry stems from the interactions of in-plane material expansion and material flow driven by the tool head. As the feed material is pushed downward and plasticized due to frictional heating, it expands beneath the tool head. With in-plane motion of the tool head, this expansion favors the trailing side over the leading side (see Fig. 14(b)). The shear forces introduced by the rotating tool head cause counterclockwise flow of the material (in the direction of tool head rotation). As illustrated in Fig. 14(c), the influx of material traveling from the trailing edge to the advancing side creates a larger and wider accumulation of material on the advancing side of the deposit. To compare, the influx of the deposited material traveling from the advancing side to the retreating side experiences low in-plane constraint with free space beneath the tool. Therefore, less material accumulation is on the retreating side. The different level of material accumulation between the advancing and retreating side is the origin of the observed asymmetry in the transverse cross-section.

The difference between the advancing and retreating side is further enhanced due to the presence of the tool protrusions. During tool rotation, the deposited material that is pushed away by the tool protrusions will accumulate right outside the tool protrusion-affected zone.

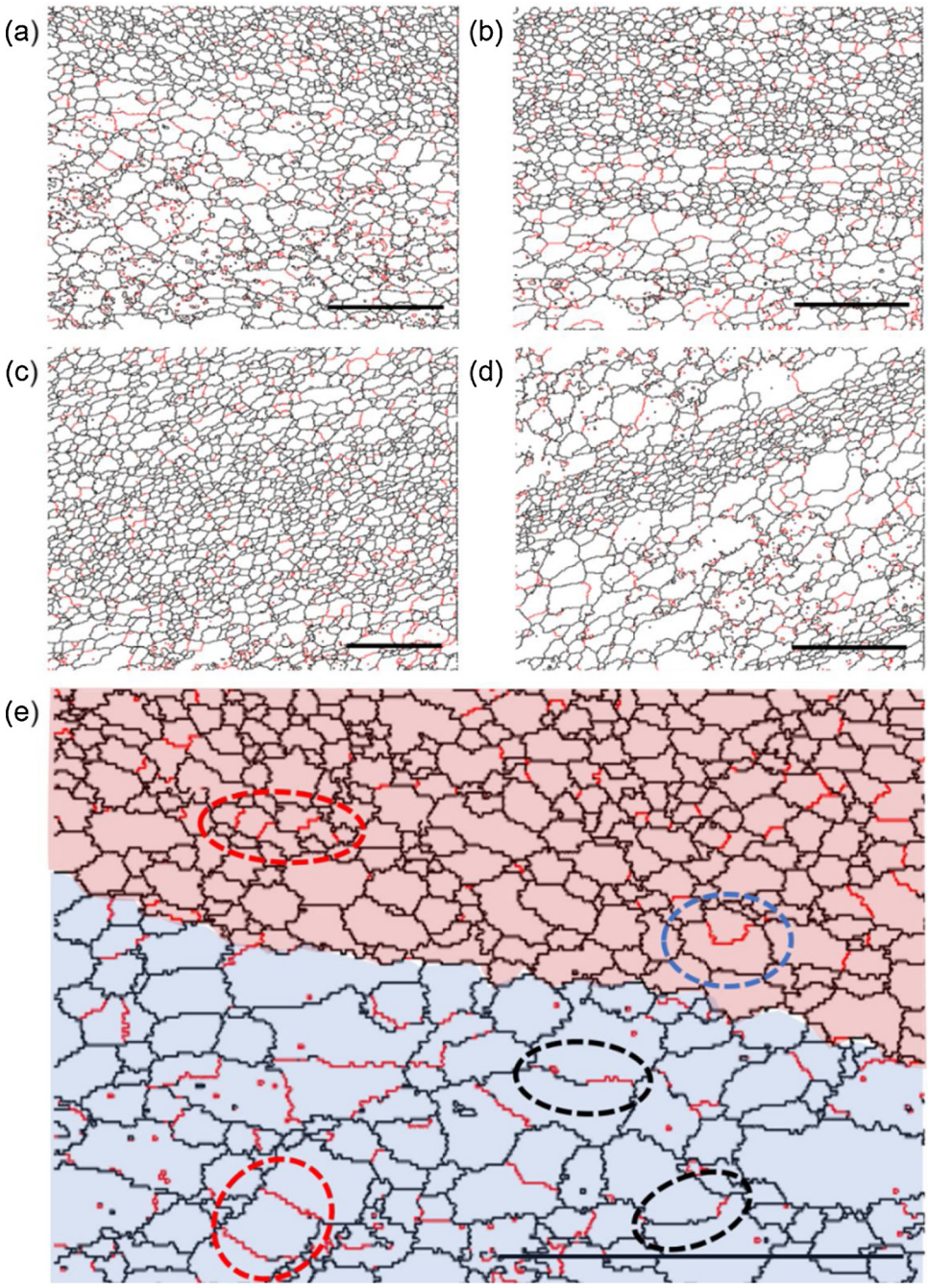

Fig. 12. (a)–(d) Misorientation maps for interfacial regions. (a) Area 1, (b) Area 2, (c) Area 3, (d) Area 4, (e) A zoomed-in image of the upper-left corner of (a). LABs (2-15 degrees) shown in red and HABs (> 15 degrees) shown in black. Scale bars in subfigures are 50 μm.

With the strong in-plane constraint from the excess material on the advancing edge, the accumulated material is forced to move synergistically with the substrate material outside the tool protrusion-affected zone. The AA 6061 substrate motion is in the outward and upward direction, so the motion of the accumulated AA 2024 is in the inward and downward direction. This leads to higher degrees of vertical mixing and fin structure formation outside the tool protrusion-affected zone on the advancing side. On the retreating side, with weak in-plane constraint and less material accumulation, no 3D structures like fins are formed.

During AFSD, the rotating tool protrusions mill temporary trenches into the uplifted substrate material around them. In areas of high in-plane constraint (i.e., from the trailing side to the advancing side), the deposited material near the protrusions will move downward to rapidly fill these trenches. This results in the serration structures seen at the interface in Figs. 3 and 4. We find that the slope of the serrations seen in the longitudinal cross-section (e.g., Fig. 4(a)) is in parallel with the outer surface of the protrusions, which further supports the view that the serrations are caused by direct interactions of the material with the tool protrusions.

5.2. Correlation of the interfacial morphology and microstructure distribution

From Section 4, the refined, equiaxed microstructure of AA 2024 is similar among Areas 1–4, suggesting that the deposited material at the interfacial regions has a similar temperature and deformation history across the deposition width—at least within the feed-rod zone and tool

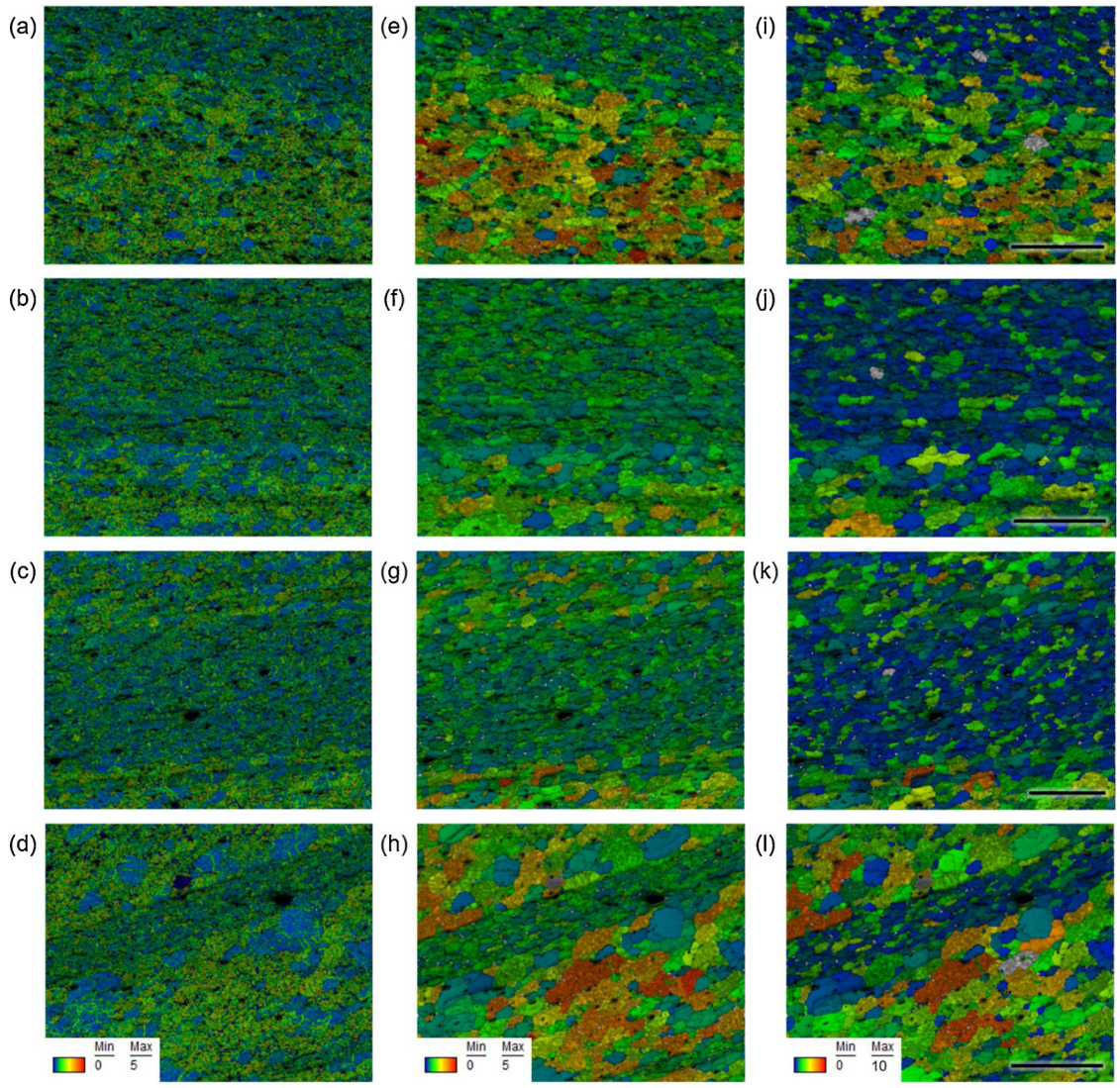

Fig. 13. EBSD maps for interfacial regions. (a)–(d) Kernel average misorientation (KAM) maps, (e)–(h) grain average misorientation (GAM) maps, and (i)–(l) grain orientation spread (GOS) maps for Areas 1–4. Scale bars in subfigures are 50 μm.

protrusion-affected zone. For the AA 6061 substrate, the interfacial regions develop a partially recrystallized microstructure. In a previous AFSD study that uses AA 6061 as the feed material, a near complete recrystallization microstructure has been observed [55]. Since the HAB fraction and the degree of recrystallization increase with strain in continuous dynamic recrystallization, this suggests that the substrate surface generally experiences less deformation than the deposited material. Moreover, the GAM/GOS maps in Fig. 13 show that Area 2 has a higher degree of recrystallization with lower intra-granular misorientation than Area 1 and Area 4. Therefore, the substrate surface away from the center of deposition should experience less deformation than that at the center of deposition. This is expected because the latter experiences more significant compression and shear due to the direct interaction with the feed-rod.

From the microstructure evolution perspective, the material in AFSD experiences two stages: (i) a short deformation stage ($\sim$ 0.1 s or less) featuring high strain and high temperature, and (ii) a relatively long annealing stage (tens of seconds) that is characterized by a gradual decrease of the temperature in the absence of external stresses. After the deformation stage, static recovery and recrystallization can occur if there is a high enough driving force from the residual dislocations and stored mechanical energy. Static recovery will lead to sharper boundaries and transform the non-equilibrium grain boundaries into equilibrium ones, while static recrystallization will form new dislocation-free grains in the regions of high dislocation density. The observed microstructures here are after both deformation and annealing stages; in principle, the exact dynamic microstructure evolution mechanisms can only be elucidated by 'freezing' the microstructure right after the deposition stage [52,56]. However, it is still reasonable to conclude that the recrystallized microstructures here are mainly from continuous dynamic recrystallization based on the misorientation mapping results and the prevalence of LABs in AA 6061.

6. Conclusions

To summarize, we have systematically investigated the interface formed in AFSD via morphological and microstructural analyses of a dissimilar Al alloy system, AA 2024 deposition onto AA 6061 substrate. The most salient findings of this work include:

- AFSD results in a non-planar interface with significant macroscopic mixing between the deposited material and the substrate observed in the out-of-plane direction. The deposited material inserts below the initial substrate surface in the feed-rod zone, while the substrate surface surges above it in the tool protrusion-affected zone.
- Interesting 3D features like fins and serrations form on the

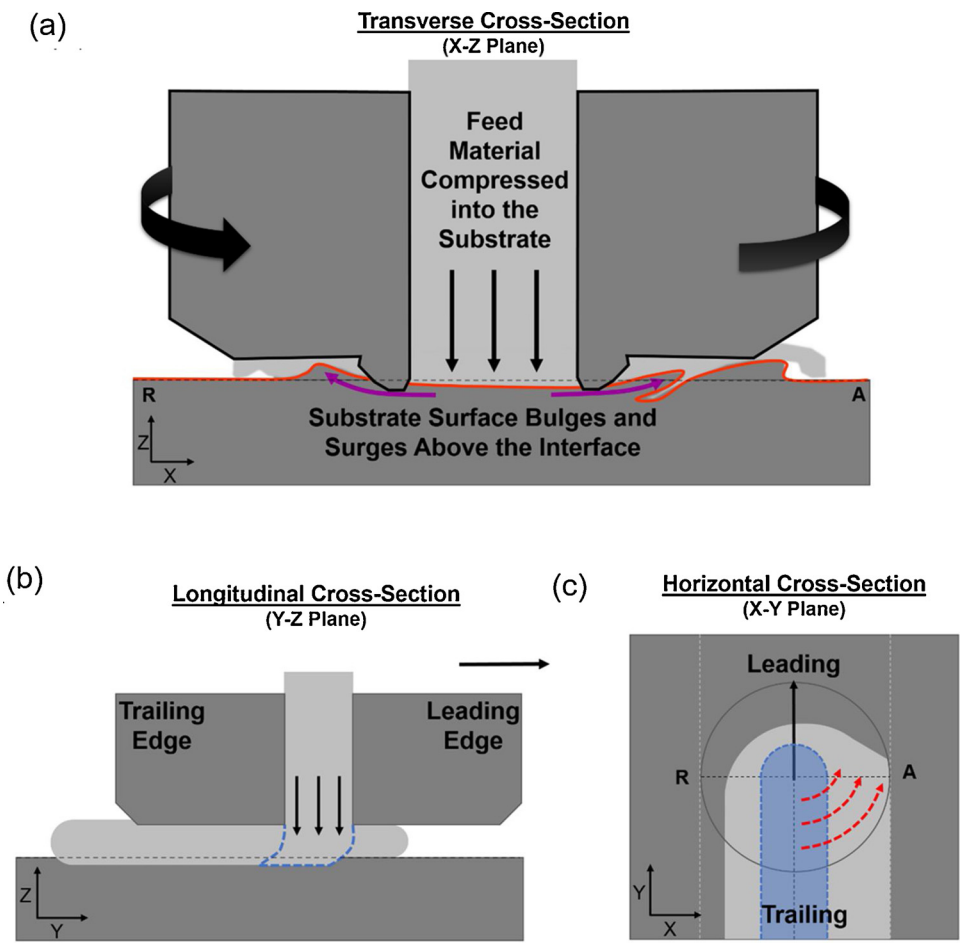

Fig. 14. (a) Transverse cross-section of the deposition showing the interfacial material flow processes. (b) Longitudinal cross-section showing mechanism for feed-rod bending and shearing due to forces created by tool in-plane motion. The dotted line represents a possible shape for the plasticized materials to deform and flow out from the feed-rod zone. (c) Horizontal cross-section showing a top-down view of the deposition process. Area in light gray correpsonds to the deposition track. Area shaded in blue corresponds to the initial addition of material via the mechanism shown in (b). Curved arrows show the direction of material flow after entering the deposition. A = advancing, R = retreating.

advancing side and lead to structural interlocking. However, the interface manifests as a smooth sloped surface on the retreating side. This asymmetry stems from the interactions of the in-plane material expansion (driven by the feeding compression) and the material flow (driven by the tool head rotation), which lead to a higher level of material accumulation and constraint on the advancing side.

- During AFSD, both the deposited AA 2024 and AA 6061 substrate surface show significant grain refinement caused by continuous dynamic recrystallization, which is characterized by dynamic recovery and subgrain formation followed by a strain-induced gradual change from LABs to HABs. The deposited AA 2024 shows an almost fully recrystallized microstructure that is similar throughout the interfacial regions. This suggests that all the deposited material has a similar thermomechanical history with large deformation.
- The substrate surface of AA 6061 shows a partially recrystallized microstructure with more intra-granular orientation gradients observed in regions that are further away from the centerline of the deposition. These regions have a lower degree of recrystallization and less deformation during AFSD than the substrate surface that is directly below the feed-rod.

We note that the exact interface morphology and microstructure depend on the material properties as well as the tool geometry. In this work, the tool head has two small protrusions on the bottom surface. For other tool geometries such as flat tools or tools with multiple larger features such as in reference [55], substantially different interfaces may arise due to expected differences in effective strain and heat generation. Understanding the influence of tool geometry on the interface morphology and microstructure is of interest for future AFSD research.

Declaration of Competing Interest

The authors declare that they have no known competing financial interests or personal relationships that could have appeared to influence the work reported in this paper.

Acknowledgements

The authors would like to thank the support from Virginia Tech-ARL CRADA (#16-13) and National Science Foundation (CMMI-1853893). The authors would like to thank Hunter Rauch for helpful discussions and Jake Yoder for assistance in experiments. MEJP would like to acknowledge the support by the National Science Foundation Graduate Research Fellowship Program. Any opinions, findings, and conclusions or recommendations expressed in this material are those of the authors and do not necessarily reflect the views of the National Science Foundation.

Appendix A. Supplementary data

Supplementary material related to this article can be found, in the online version, at doi:https://doi.org/10.1016/j.addma.2020.101293.

References

[1] H.Z. Yu, et al., Non-beam-based metal additive manufacturing enabled by additive friction stir deposition, Scr. Mater. 153 (2018) 122–130 2018/04/07/.
[2] R.J. Griffiths, et al., A perspective on solid-state additive manufacturing of aluminum matrix composites using MELD, J. Mater. Eng. Perform. 28 (2) (2019) 648–656 February 01.
[3] A. Simar, Y. Bréchet, B. de Meester, A. Denquin, C. Gallais, T. Pardoen, Integrated

modeling of friction stir welding of 6xxx series Al alloys: process, microstructure and properties, Prog. Mater. Sci. 57 (1) (2012) 95–183 2012/01/01/.
[4] P.L. Threadgill, A.J. Leonard, H.R. Shercliff, P.J. Withers, Friction stir welding of aluminium alloys, Int. Mater. Rev. 54 (2) (2009) 49–93 2009/03/01.
[5] W. Woo, et al., In situ neutron diffraction measurements of temperature and stresses during friction stir welding of 6061-T6 aluminium alloy, Sci. Technol. Weld. Join. 12 (4) (2007) 298–303 2007/05/01.
[6] R. Kumar, V. Pancholi, R.P. Bharti, Material flow visualization and determination of strain rate during friction stir welding, J. Mater. Process. Technol. 255 (2018) 470–476 2018/05/01/.
[7] F.C. Liu, Y. Hovanski, M.P. Miles, C.D. Sorensen, T.W. Nelson, A review of friction stir welding of steels: tool, material flow, microstructure, and properties, J. Mater. Sci. Technol. (2017) 2017/11/01/.
[8] Y. Morisada, T. Imaizumi, H. Fujii, Determination of strain rate in Friction stir Welding by three-dimensional visualization of material flow using X-ray radiography, Scr. Mater. 106 (2015) 57–60 2015/09/01/.
[9] O.G. Rivera, et al., Influence of texture and grain refinement on the mechanical behavior of AA2219 fabricated by high shear solid state material deposition, Mater. Sci. Eng. A 724 (2018) 547–558 2018/05/02/.
[10] R.S. Mishra, Z.Y. Ma, Friction stir welding and processing, Mater. Sci. Eng. R Rep. 50 (1) (2005) 1–78 2005/08/31/.
[11] J. P. Schultz, K. D. Creehan, Fabrication tools for exerting normal forces on feedstock, Google Patents, 2017.
[12] O.G. Rivera, et al., Microstructures and mechanical behavior of Inconel 625 fabricated by solid-state additive manufacturing, Mater. Sci. Eng. A 694 (2017) 1–9 2017/05/10/.
[13] A. Basak, S. Das, Epitaxy and microstructure evolution in metal additive manufacturing, Annu. Rev. Mater. Res. 46 (1) (2016) 125–149.
[14] W.E. Frazier, Metal additive manufacturing: a review, J. Mater. Eng. Perform. 23 (6) (2014) 1917–1928 June 01.
[15] Y. Kok, et al., Anisotropy and heterogeneity of microstructure and mechanical properties in metal additive manufacturing: a critical review, Mater. Des. 139 (2018) 565–586 2018/02/05/.
[16] M. Tang, P.C. Pistorius, Anisotropic mechanical behavior of AlSi10Mg parts produced by selective laser melting, JOM 69 (3) (2017) 516–522 March 01.
[17] G. Nicoletto, Anisotropic high cycle fatigue behavior of Ti–6Al–4V obtained by powder bed laser fusion, Int. J. Fatigue 94 (2017) 255–262 2017/01/01/.
[18] A.E. Wilson-Heid, S. Qin, A.M. Beese, Anisotropic multiaxial plasticity model for laser powder bed fusion additively manufactured Ti-6Al-4V, Mater. Sci. Eng. A 738 (2018) 90–97 2018/12/19/.
[19] B.E. Carroll, T.A. Palmer, A.M. Beese, Anisotropic tensile behavior of Ti–6Al–4V components fabricated with directed energy deposition additive manufacturing, Acta Mater. 87 (Supplement C) (2015) 309–320 2015/04/01/.
[20] M. Simonelli, Y.Y. Tse, C. Tuck, Effect of the build orientation on the mechanical properties and fracture modes of SLM Ti–6Al–4V, Mater. Sci. Eng. A 616 (2014) 1–11 2014/10/20/.
[21] J.R. Calvert, Microstructure and Mechanical Properties of WE43 Alloy Produced Via Additive Friction STIR TECHNOLOGY, Master of Science, Materials Science and Engineering Virginia Polytechnic Institute and State University, Blacksburg, VA, 2015.
[22] D.Z. Avery, et al., Fatigue behavior of solid-state additive manufactured inconel 625, JOM 70 (11) (2018) 2475–2484 2018/11/01.
[23] R.J. Griffiths, et al., Additive friction stir-enabled solid-state additive manufacturing for the repair of 7075 aluminum alloy, Appl. Sci. 9 (17) (2019) 3486.
[24] R. Nandan, G.G. Roy, T.J. Lienert, T. Debroy, Three-dimensional heat and material flow during friction stir welding of mild steel, Acta Mater. 55 (3) (2007) 883–895.
[25] S. Xu, X. deng, A.P. Reynolds, T.U. Seidel, Finite element simulation of material flow in friction stir welding, Sci. Technol. Weld. Join. 6 (3) (2001) 191–193.
[26] N. Dialami, M. Chiumenti, M. Cervera, C. Agelet de Saracibar, J.P. Ponthot, Material flow visualization in friction stir welding via particle tracing, Int. J. Mater. Form. 8 (2) (2015) 167–181. April 01.
[27] P.D. Edwards, M. Ramulu, Material flow during friction stir welding of Ti-6Al-4V, J. Mater. Process. Technol. 218 (2015) 107–115 2015/04/01/.
[28] R. Fonda, D.J. Rowenhorst, K. Knipling, 3D Material Flow in Friction Stir Welds, (2018).
[29] B.T. Gibson, W. Tang, A.G. Peterson, Z. Feng, G.J. Frederick, Evaluating the potential for remote in-process monitoring of tool wear in friction stir welding of stainless steel, J. Manuf. Sci. Eng. 140 (2) (2017) 21012–021012–11.
[30] Y. Huang, et al., Material-Flow Behavior During Friction-Stir Welding of 6082-T6 Aluminum Alloy, (2016).
[31] H. Khalid Rafi, G. Phanikumar, K. Prasad Rao, Material flow visualization during friction surfacing, Metall. Mater. Trans. A 42 (4) (2011) 937–939. April 01.
[32] W.-Y. Li, J.-F. Li, Z.-H. Zhang, D.-L. Gao, Y.-J. Chao, Metal flow during friction stir welding of 7075-T651 aluminum alloy, Exp. Mech. 53 (9) (2013) 1573–1582 November 01.
[33] X.C. Liu, Y.F. Sun, Y. Morisada, H. Fujii, Dynamics of rotational flow in friction stir welding of aluminium alloys, J. Mater. Process. Technol. 252 (2018) 643–651 2018/02/01/.
[34] O. Lorrain, V. Favier, H. Zahrouni, D. Lawrjaniec, Understanding the material flow path of friction stir welding process using unthreaded tools, J. Mater. Process. Technol. 210 (4) (2010) 603–609 2010/03/01/.
[35] Y. Morisada, H. Fujii, Y. Kawahito, K. Nakata, M. Tanaka, Three-dimensional visualization of material flow during friction stir welding by two pairs of X-ray transmission systems, Scr. Mater. 65 (12) (2011) 1085–1088 2011/12/01/.
[36] S. Pandya, R.S. Mishra, A. Arora, Channel formation during friction stir channeling process — a material flow study using X-Ray micro-computed tomography and optical microscopy, J. Manuf. Process. 41 (2019) 48–55 2019/05/01/.
[37] A.P. Reynolds, Flow visualization and simulation in FSW, Scr. Mater. 58 (5) (2008) 338–342 2008/03/01/.
[38] A. Tongne, C. Desrayaud, M. Jahazi, E. Feulvarch, On material flow in friction stir welded Al alloys, J. Mater. Process. Technol. 239 (2017) 284–296 2017/01/01/.
[39] Q. Yang, S. Mironov, Y.S. Sato, K. Okamoto, Material flow during friction stir spot welding, Mater. Sci. Eng. A 527 (16) (2010) 4389–4398 2010/06/25/.
[40] F.J. Humphreys, M. Hatherly, Chapter 13 - Hot deformation and dynamic restoration, in: F.J. Humphreys, M. Hatherly (Eds.), Recrystallization and Related Annealing Phenomena, second edition), Elsevier, Oxford, 2004pp. 415-V.
[41] F.J. Humphreys, M. Hatherly, Chapter 14 - continuous recrystallization during and after large strain deformation, in: F.J. Humphreys, M. Hatherly (Eds.), Recrystallization and Related Annealing Phenomena, second edition), Elsevier, Oxford, 2004, pp. 451–467.
[42] H. Izadi, J. Fallu, A. Abdel-Gwad, T. Liyanage, A.P. Gerlich, Analysis of tool geometry in dissimilar Al alloy friction stir welds using optical microscopy and serial sectioning, Sci. Technol. Weld. Join. 18 (4) (2013) 307–313 2013/05/01.
[43] Y. Li, L.E. Murr, J.C. McClure, Flow visualization and residual microstructures associated with the friction-stir welding of 2024 aluminum to 6061 aluminum, Mater. Sci. Eng. A 271 (1) (1999) 213–223 1999/11/01/.
[44] M.M. Corporation, Meld Manufacturing, Available: (2019) http://meldmanufacturing.com/.
[45] Z.W. Chen, S. Cui, On the forming mechanism of banded structures in aluminium alloy friction stir welds, Scr. Mater. 58 (5) (2008) 417–420 2008/03/01/.
[46] G.R. Cui, Z.Y. Ma, S.X. Li, Periodical plastic flow pattern in friction stir processed Al–Mg alloy, Scr. Mater. 58 (12) (2008) 1082–1085 2008/06/01/.
[47] K.N. Krishnan, On the formation of onion rings in friction stir welds, Mater. Sci. Eng. A 327 (2) (2002) 246–251 2002/04/30/.
[48] A. Tongne, M. Jahazi, E. Feulvarch, C. Desrayaud, Banded structures in friction stir welded Al alloys, J. Mater. Process. Technol. 221 (2015) 269–278 2015/07/01/.
[49] J.K. MACKENZIE, Second Paper on statistics associated with the RANDOM DISORIENTATION OF CUBES, Biometrika 45 (1–2) (1958) 229–240.
[50] X.C. Liu, Y.F. Sun, H. Fujii, Clarification of microstructure evolution of aluminum during friction stir welding using liquid CO2 rapid cooling, Mater. Des. 129 (2017) 151–163 2017/09/05/.
[51] T. Sakai, A. Belyakov, R. Kaibyshev, H. Miura, J.J. Jonas, Dynamic and post-dynamic recrystallization under hot, cold and severe plastic deformation conditions, Prog. Mater. Sci. 60 (2014) 130–207 2014/03/01/.
[52] S. Mironov, K. Inagaki, Y.S. Sato, H. Kokawa, Microstructural evolution of pure copper during friction-stir welding, Philos. Mag. 95 (4) (2015) 367–381 2015/02/01.
[53] U.F.H.R. Suhuddin, S. Mironov, Y.S. Sato, H. Kokawa, Grain structure and texture evolution during friction stir welding of thin 6016 aluminum alloy sheets, Mater. Sci. Eng. A 527 (7) (2010) 1962–1969 2010/03/25/.
[54] T.R. McNelley, S. Swaminathan, J.Q. Su, Recrystallization mechanisms during friction stir welding/processing of aluminum alloys, Scr. Mater. 58 (5) (2008) 349–354 2008/03/01/.
[55] B.J. Phillips, et al., Microstructure-deformation relationship of additive friction stir-deposition Al–Mg–Si, Materialia 7 (2019) 1003872019/09/01/.
[56] X.C. Liu, Y.F. Sun, T. Nagira, K. Ushioda, H. Fujii, Evaluation of dynamic development of grain structure during friction stir welding of pure copper using a quasi in situ method, J. Mater. Sci. Technol. 35 (7) (2019) 1412–1421 2019/07/01/.